

# Theoretical investigation of droplet splitting due to electrowetting on dielectric in a Hele-Shaw cell

メタデータ	言語: English 出版者: AIP Publishing 公開日: 2022-10-18 キーワード (Ja): キーワード (En): 作成者: 加藤, 健司, 脇本, 辰郎, 伊藤, 高啓, 松浦, 丈夫 メールアドレス: 所属: Osaka City University, Osaka City University, Chubu University, Osaka City University
URL	<a href="https://ocu-omu.repo.nii.ac.jp/records/2020427">https://ocu-omu.repo.nii.ac.jp/records/2020427</a>

# Theoretical investigation of droplet splitting due to electrowetting on dielectric in a Hele–Shaw cell

Kenji Katoh, Tatsuro Wakimoto, Takahiro Ito, Jyobu Matsuura

<b>Citation</b>	Physics of Fluids. 34(6); 062114
<b>Issue Date</b>	2022-06
<b>Type</b>	Journal Article
<b>Textversion</b>	Author
<b>Rights</b>	© 2022 Authors. Published under an exclusive license by AIP Publishing. This is the accept manuscript version. This article may be downloaded for personal use only. Any other use requires prior permission of the author and AIP Publishing. This article appeared in Physics of Fluids, Vol.34, Issu.6 and may be found at <a href="https://doi.org/10.1063/5.0095846">https://doi.org/10.1063/5.0095846</a> .
<b>DOI</b>	10.1063/5.0095846

Self-Archiving by Author(s)  
Placed on: Osaka City University Repository

**Title:**

Theoretical investigation of Droplet splitting due to electrowetting on dielectric in a Hele-Shaw cell

**Author names and affiliations:**

Kenji Katoh<sup>1</sup>, Tatsuro Wakimoto<sup>1</sup>, Takahiro Ito<sup>2</sup> and Jyobu Matsuura<sup>1</sup>

1. Department of Mechanical Engineering, Osaka City University, 3-3-138 Sugimoto Sumiyoshi-ku, Osaka 558-8585, Japan
2. Department of Mechanical Engineering, Chubu University, 1200, Matsumoto-cho, Kasugai, 487-8501, Japan

**Corresponding author:**

Kenji Katoh

Phone: +81-6-6605-2665, Fax: +81-6-6605-2953

E-mail: katoh@ osaka-cu.ac.jp

**Abstract**

An experimental and theoretical study was conducted to investigate the electrowetting on dielectric (EWOD)-induced splitting behavior of droplets placed in a Hele-Shaw cell. The deformation behavior of the droplet was experimentally observed under various applied voltages. A theoretical model was proposed to express the droplet behavior by balancing the surface tension, viscous force, and pressure acting on the droplet. The effect of the dynamic contact angle was considered and used to estimate the capillary force along on the moving contact line. The results obtained from the theoretical model showed a qualitative agreement with the deformation behavior of the observed droplets. An approximate model was proposed to verify observations that showed that the contact line widths at the boundary between positive and negative electrodes remain almost constant during the splitting process. The behavior of the contact line width was explained by the model, based on the minimum work required for droplet deformation during the splitting process.

**I. INTRODUCTION**

Recently, there has been a growing demand for devices which can control the movement of droplets on the wall surface, as used in microfluidics or in lab-on-a-chip technology. Several methods have been proposed to manipulate droplets, using the change in the surface tension, or the wettability between the droplet and wall<sup>1-6</sup>. Electrowetting on dielectric (EWOD)<sup>7,8</sup>, where the wettability changes depending on the electric field, is attracting attention because of its low power consumption and large change in wettability. Numerous studies about application of EWOD have been conducted to

investigate the transportation of test liquids, enabling the development of various devices such as optical lenses, electronic paper, and condensers<sup>9-21</sup>.

Many experimental and numerical investigations have been conducted on the dynamics of droplets on the wall surface, driven by EWOD. Oh *et al.*<sup>22,23</sup> experimentally investigated droplet deformation under a given electric field. Additionally, Ko *et al.*<sup>24</sup> measured the velocity field of a droplet driven by EWOD using a flow visualization technique. Lu *et al.*<sup>25</sup> conducted an experimental and numerical study on the movement and splitting of droplets placed in a Hele-Shaw cell with a gap between the two flat plates. The deformation of the triple-phase contact line, and the change in the contact angle during movement or splitting of the droplet, were observed experimentally. Their numerical results, based on the diffuse-interface model, qualitatively agreed with the observed droplet motion. Izadi & Moosavi<sup>26</sup> used a similar method to perform a numerical analysis of droplet movement in non-Newtonian liquids. Similarly, Li *et al.*<sup>27</sup> performed a numerical simulation using the front-tracking method to capture the interface of a droplet in a Hele-Shaw cell. Guan *et al.*<sup>28</sup> performed numerical calculations using the volume of fluid (VOF) and level set methods. Wang *et al.*<sup>29</sup> used the level set method to numerically analyze the droplet splitting behavior in a Hele-Shaw cell with a partition plate. Although their numerical methods successfully reproduced the observed droplet behavior, no consideration was made for the dynamic wetting, that is, the contact angle dependent on the velocity of the triple-phase contact line. Yamamoto *et al.*<sup>30</sup> used the generalized Navier boundary condition (GNBC) as the sliding boundary condition for the wall surface, considering the velocity's dependence of the contact angle. By applying a fitting parameter to the relationship between the slip velocity of the contact line and the contact angle, they obtained numerical results that were similar to the observed droplet behavior. However, in the method used by Yamamoto *et al.*<sup>30</sup>, the fitting parameters used had a physical basis that was unclear. To elucidate droplet motion driven by EWOD, it is necessary to build a theoretical model that employs only the observed parameters, and not the fitting parameters.

In this study, we experimentally and theoretically examined the EWOD-induced splitting behavior of droplets placed in a Hele-Shaw cell similar to those treated in the above studies. In the previous report (Yamamoto *et al.*<sup>30</sup>), the authors of this paper conducted a theoretical analysis of droplet movement using a relatively simple model that was based on the force balance between the capillary force and the viscous force. The theoretical results were in agreement with the experimental results for simple movement of droplet without splitting observed by Lu *et al.*<sup>25</sup>. In this study, we designed test plate that exhibited the EWOD effect, enabling the observation of the droplet splitting process for various applied voltages. A theoretical model is proposed to describe the droplet behavior during splitting, taking into consideration the dependence of the contact angle on the contact line velocity, as observed in the experiment. The equation of motion was derived from a balance between the pressure, viscous force, and surface tension force, considering the effect of dynamic wetting. The

validity of the proposed model was examined by comparing the change in the droplet shape observed experimentally with that obtained from the theoretical model. The proposed theoretical model suggests that the contact line width at the boundary between the positive and negative electrodes of the EWOD substrate has a significant effect on the driving force that moves the droplet. The change in the contact line width was estimated using an approximate model. We showed that the actual contact line width should be determined using the condition of minimum work during droplet deformation.

## II. EXPERIMENTAL METHOD

Before describing the experimental equipment used in this study, the EWOD principle is briefly explained. Figure 1 shows a schematic of a droplet placed on an electrode substrate coated with a dielectric thin film between the positive and negative electrodes. When a voltage is applied to the system shown in Fig. 1, the wettability of the positive electrode is improved, and the contact angle decreases from  $\theta_0$  to  $\theta$ . The decrease in the contact angle can be determined using the Young-Lippmann equation shown below<sup>8</sup>.

$$\cos \theta - \cos \theta_0 = \frac{CV^2}{2\sigma}. \quad (1)$$

Here,  $C$  is the capacitance of the dielectric thin film per unit area of the wall surface,  $V$  is the voltage, and  $\sigma$  is the surface tension of the liquid. As shown in Fig. 1, the tangential component of the surface tension acting on the droplet is larger on the positive electrode, and as a result, the droplet moves toward the positive electrode side.

### A. Experimental apparatus

Figure 2 shows an outline of the experimental equipment used in this study. The experimental system is similar to that treated by Lu et al.<sup>25</sup>. A Hele-Shaw cell was constructed with the gap of  $b=0.53$  mm between the upper and lower substrates. The upper substrate was a cathode, and the lower

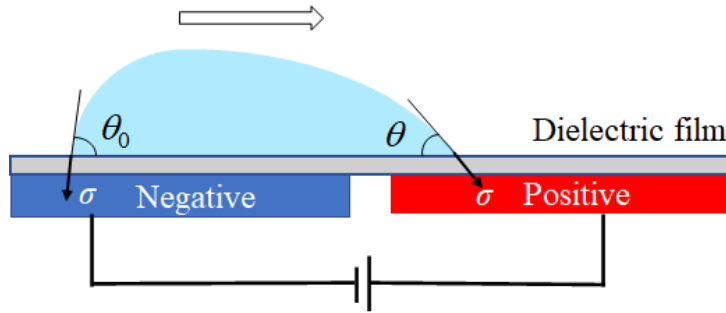


Figure 1 Droplet driven by EWOD when voltage is applied to electrode with dielectric film.

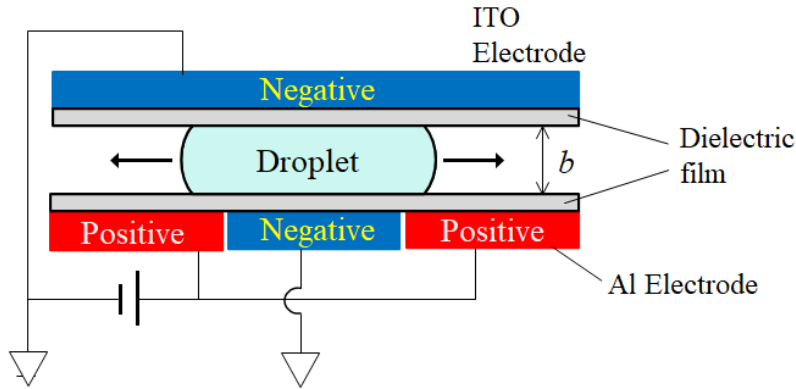


Figure 2 Schematic of experimental equipment to observe splitting of droplet in Hele-Shaw cell composed of EWOD electrodes.

substrate was composed of three electrodes. One of them was a cathode sandwiched between two positive electrodes. A dielectric thin film was applied to each electrode surface. When a voltage was applied, the wettability of the positive electrode on the lower substrate improved, and the droplets moved toward the positive electrodes on both sides, eventually splitting. To enable the observation of the behavior of the droplets in the cell, from above, a glass coated with a transparent indium tin oxide (ITO) conductive thin film, was used as the upper substrate, as shown in Fig. 2. A glass plate, with aluminum vapor deposition (approximately 100 nm thick), was used as the lower substrate.

The lower substrate surface was coated with a photoresist solution, and a square-shaped mask was attached. A 10 mm square aluminum electrode was etched on a glass substrate, by isolating the aluminum in the electrode area, and removing the rest. To make the effect of EWOD more visible, it is necessary to install a dielectric thin film with high water repellency and large capacitance, on the upper and lower substrates. In this experiment, a dielectric thin film, Cytop (AGC corp., solvent: CTL-107MK), was applied to the upper and lower substrates, using the dip-coating method. The substrate was vertically immersed and withdrawn from a Cytop solution at a constant speed of 60 mm/min, using a linear cylinder. After drying, the substrate was kept in an electric furnace at 170 °C for 50 minutes to remove the excess solvent, and form a uniform thin film. All operations were performed in a simple clean room. To increase the change in the contact angle due to EWOD, it is necessary to increase the difference in capacitance between the upper and lower substrates. In this experiment, the concentration of the solution was adjusted so that the Cytop film thickness of the lower substrate was approximately 10 times thicker than that of the upper substrate. The thin film thicknesses of the upper and lower substrates were approximately 100 nm and 1000 nm, respectively.

If pinholes are present on the surface due to the non-uniformity of the dielectric thin film created on the substrate surface, the leakage current flowing in the droplet cannot be ignored. Consequently, the decrease in the voltage applied to the dielectric film may reduce the EWOD effect locally. To

Table 1 Properties of the 80% glycerol solution and static contact angle to the electrode at a temperature of  $20 \pm 0.5^\circ\text{C}$ .

$\rho$ (kg/m <sup>3</sup> )	$\sigma$ (N/m)	$\mu$ (Pa · s)	$\theta_A$ (deg)	$\theta_R$ (deg)
1211 $\pm$ 1	0.0665 $\pm$ 0.0003	0.058 $\pm$ 0.001	104.7 $\pm$ 0.5	98.8 $\pm$ 0.5

improve the homogeneity of the thin film, the substrate surface was activated by exposing it to ultraviolet (UV) rays for 24 hours, before forming a thin film using the dip-coating method. By irradiating with UV irradiation, it was confirmed that the contact lines of the droplets were not distorted during deformation, achieving a smooth motion. Considering the withstand voltage of the dielectric thin film used in this experiment, the movement and splitting of the droplets were experimentally observed in the range of 60 to 80 V. Within this voltage range, the leakage current in the thin film was measured using a micro ammeter (Picoammeter Model 6485 manufactured by Keithley). The leakage current was approximately 20 nA/mm<sup>2</sup> when not irradiated with ultraviolet rays, and decreased to 1 nA/mm<sup>2</sup> or less after irradiation. It was confirmed that the effect of the leakage current on splitting process can be ignored.

## B. Measurement of substrate capacitance and contact angles

An aqueous 80% glycerol solution, at a temperature of  $20 \pm 0.5^\circ\text{C}$ , was used as the test liquid. The density  $\rho$ , surface tension  $\sigma$ , and viscosity  $\mu$ , were measured using Boume's hydrometer, Wilhelmy's tensiometer, and Ubbelohde viscometer, respectively. Table 1 shows the physical properties and measurement results of the quasi-static advancing and receding contact angles,  $\theta_A$  and  $\theta_R$ , with respect to the substrate. The contact angle was determined from the photographed image of the gas-liquid interface near the wall surface. The position of the gas-liquid interface was determined based on the pixel with the highest brightness gradient; and the contact angle was obtained from the wall gradient of the interface curve, approximated using the quadratic curve, from the wall to a height of approximately 0.1 mm. For the quasi-static advancing and receding contact angles  $\theta_A$  and  $\theta_R$  shown in Table 1, the measurement was repeated six times, under the condition that the contact line velocity was 0.01 mm/s or less; therefore, the influence of the contact line velocity was negligible. The uncertainty in the contact angle measurement was approximately  $\pm 0.5^\circ$ .

Figure 3 shows a schematic, and an equivalent electric circuit, when the voltage  $V_0$  is applied to the experimental system.  $C'$  and  $C$  are the capacitances per unit area of the upper and lower substrates, respectively,  $S$  is the total droplet adhesion area on the lower substrate, and  $S_P$  is the droplet area on the positive electrode of the lower substrate. From the equivalent circuit shown in Fig. 3, when the voltage applied is  $V_0$ , the voltage  $V$  actually applied to the dielectric film of the positive electrode that

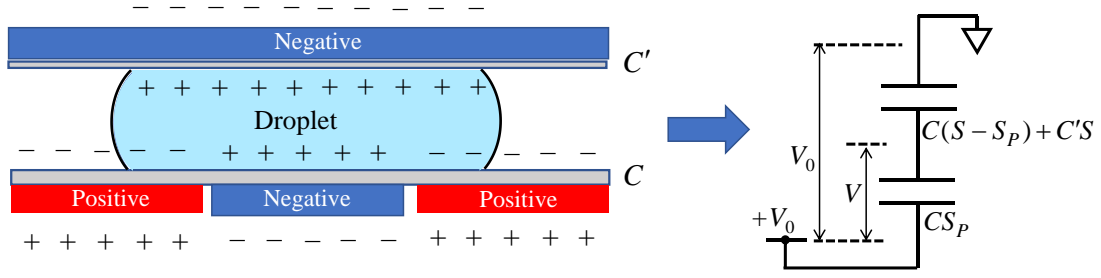


Figure 3 Schematic of the charge distribution on the substrates, and the equivalent circuit (Left figure: charge distribution; right figure: equivalent electric circuit).

contributes to the EWOD effect can be expressed as follows:

$$V = V_0 \left( 1 - \frac{C}{C + C'} \frac{S_p}{S} \right). \quad (2)$$

Here, the relationship between the capacitances  $C$  and  $C'$ , and the Cytop film thickness, can be expressed using the following equations:

$$C = \frac{\varepsilon \varepsilon_0}{d}, \quad C' = \frac{\varepsilon \varepsilon_0}{d'}, \quad (3)$$

where,  $\varepsilon_0$  is the permittivity of the vacuum, and  $\varepsilon$  is the relative permittivity of Cytop. In addition,  $d$  and  $d'$  are the Cytop film thicknesses of the upper and lower substrates, respectively. The Young-Lippmann equation (1) can now be expressed using Eqs. (2) and (3).

$$\cos \theta - \cos \theta_0 = \frac{CV^2}{2\sigma} = \frac{C}{2\sigma} \left[ V_0 \left( 1 - f \frac{S_p}{S} \right) \right]^2 \quad (4)$$

Here,  $f \left( \equiv \frac{d'}{d + d'} = \frac{C}{C + C'} \right)$ , represents the Cytop film thickness ratio between the upper and lower substrates.

To obtain the contact angle  $\theta$  from Eq. (4) at a certain area ratio ( $S_p/S$ ) during the splitting process, the capacitances  $C$  and  $C'$  should be measured to estimate the film thickness ratio  $f$ . The capacitance  $C$ , can be obtained from the change in the contact angle with respect to the applied voltage, when only the lower substrate was coated with the Cytop film. Since the positive electrode voltage  $V$  in Eq. (4) is equal to  $V_0$  in this system, we can estimate  $C$  without the influence of  $f$  or  $S_p/S$ . Similarly,  $C'$  can be obtained from the same measurement, when only the upper substrate was coated with the Cytop film. Figure 4 shows a photograph taken in the lateral direction, when the Cytop film is present on only the lower substrate. The wettability improved with the advancing contact angle, from  $104.8^\circ$

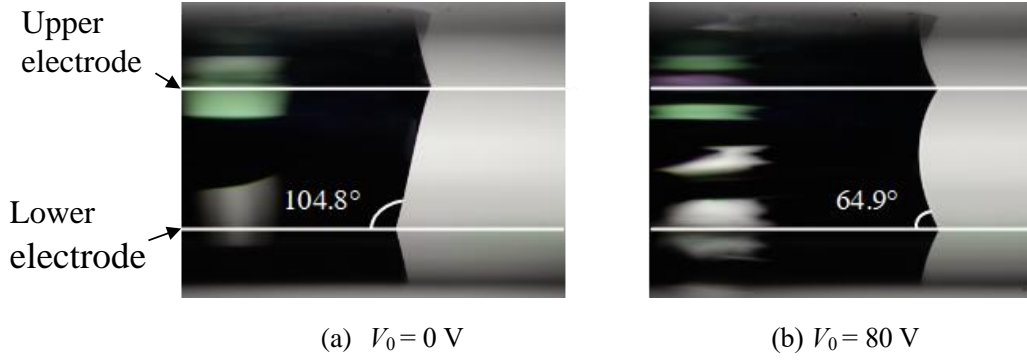


Figure 4 Change in the advancing contact angle due to the EWOD effect when voltage is applied to the positive electrode on which the droplet is placed (the images above and below the electrodes are mirror images).

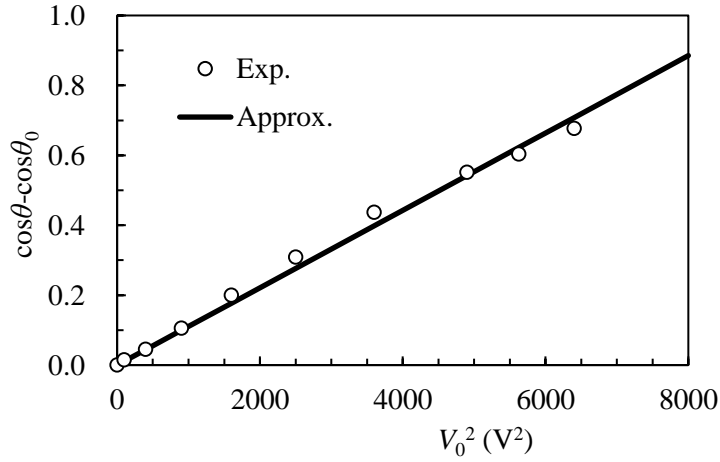


Figure 5 Relationship between  $\cos\theta - \cos\theta_0$  and  $V^2$  for the lower substrate.

at 0 V, as shown in Fig. 4 (a), to  $64.9^\circ$  at 80 V, as shown in Fig. 4 (b). Figure 5 shows the relationship between the cosine of the contact angle on the lower Cytop film, and the square of the voltage. Each plot represents an average of five measurements. The experimental results can be approximated using the Young-Lippmann equation (1).  $C/2\sigma$  in Eq. (1) was obtained from the gradient of the approximate straight line, and the capacitance  $C$  was determined.  $C'$  was measured using the same method. The capacitances of the upper and lower substrates were  $C = (1.47 \pm 0.08) \times 10^{-5} \text{ F/m}^2$ , and  $C' = (1.2 \pm 0.3) \times 10^{-4} \text{ F/m}^2$ , respectively. The Cytop film thicknesses of the upper and lower substrates were  $d \approx 1200 \text{ nm}$  and  $d' \approx 140 \text{ nm}$ , respectively, and  $f = 0.108$ . At the area ratio  $S_P/S$ , immediately before splitting of the droplet,  $V$  was about 10% smaller than  $V_0$ , which had a non-negligible effect on the value of the contact angle in Eq. (4). Since  $f \ll 1$  in this experiment, Eq. (4) was approximated as follows:

$$\cos \theta - \cos \theta_0 = \frac{CV^2}{2\sigma} = \frac{C}{2\sigma} \left[ V_0 \left( 1 - f \frac{S_P}{S} \right) \right]^2 \approx \frac{CV_0^2}{2\sigma} \left[ 1 - 2f \frac{S_P}{S} \right]. \quad (5)$$

The residual voltage ( $V_0 - V$ ) was actually imposed on the cathode of the upper substrate, as shown in Fig. 3, changing the contact angle of the upper plate slightly due to EWOD. However, because the change in the cosine of the contact angle is approximately  $f^2$  times that in Eq. (5), it can be neglected.

When the velocity of the contact line is finite, dynamic wetting occurs, and the contact angle changes with the velocity. Here, the Hoffmann-Voinov-Tanner equation is used to obtain the dynamic contact angle  $\theta_d$  from the static contact angle  $\theta_0$ <sup>30,31</sup>.

$$\theta_d = \left( \theta_0^3 + kCa \right)^{1/3}, \quad (6)$$

where  $k$  is an experimental constant, and  $Ca$  is the capillary number, which is defined as follows:

$$Ca = \frac{\mu v}{\sigma} \quad (7)$$

with  $v$  representing the velocity of the contact line (positive when advancing, and negative when receding). In this experiment,  $v$  is typically 1 mm/s, and the order of  $Ca$  is  $10^{-3}$  to  $10^{-2}$ . Linear approximation is done using the Taylor expansion in Eq. (6), and the cosine of the contact angle is obtained from the relation below<sup>30</sup>.

$$\cos \theta_0 - \cos \theta_d \approx \frac{k \sin \theta_0}{3 \theta_0^2} Ca = \frac{k \sin \theta_0}{3 \theta_0^2} \frac{\mu v}{\sigma} \quad (8)$$

Figure 6 shows the relationship between the cosine of the dynamic advancing contact angle and the moving velocity of the contact line. Each measured value represents the average of five

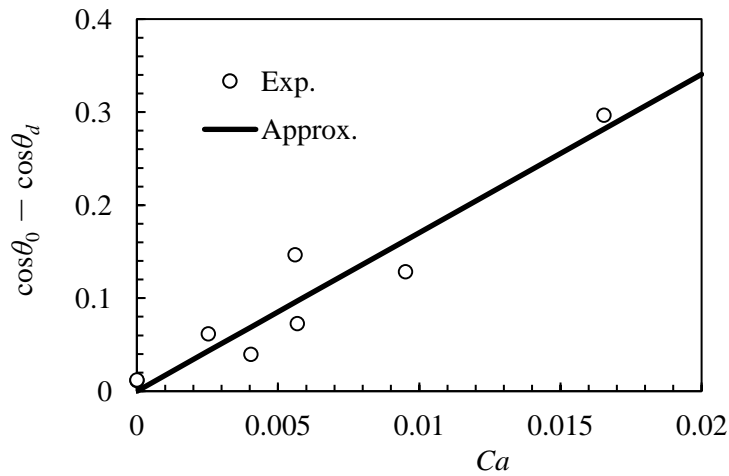


Figure 6 Relationship between the cosine of the dynamic contact angle, and the capillary number.

experiments. Despite the presence of scatter, it can be seen that the change in the cosine of the contact angle increases almost linearly with the capillary number. The value of  $k$  in Eq. (8) was obtained from the gradient of the linear approximation of the measured values, using the least-squares method. In this experiment, a value of  $k = 177 \pm 30$  was obtained. As shown in the theoretical analysis in Section 3, dynamic wetting contributes at most 30% to the total drag acting on the droplet, if the value of  $k$  mentioned above is used. Thus, the measured uncertainty of  $k$  does not significantly affect the calculations in the droplet splitting process. For example, the effect of the uncertainty of  $k$  on the calculated split time shown in Fig. 14 was less than 5%.

### III. Theoretical consideration of droplet splitting

In this section, we theoretically consider the dynamics of the droplet splitting process. Figure 7 shows a series of photographs outlining the splitting process (voltage  $V_0 = 75$  V). In this experiment, the positive and negative electrode widths were  $W = 10$  mm, and the droplet radius  $R_0$  at  $t = 0$  (initial state) in Fig. 7 was, approximately 6 mm. The time  $t$  shown in the figure represents the time that had elapsed since the voltage was applied. As shown in the figure, when the liquid flows into the two positive electrodes, the droplet is constricted at the center, and breaks at approximately  $t = 10$  s. Examining the straight line (red line in the figure), connecting the two intersections between the contact line and the positive and negative electrode boundaries, it can be seen that the length remains almost the same during the entire splitting process. Under all experimental conditions, it was observed that the width  $w$  of the contact line at the boundary between the two electrodes remained almost constant during the splitting process. From the geometry as shown in Fig. 7,  $w$  at  $t = 0$  is related to the droplet radius and electrode width as follows:

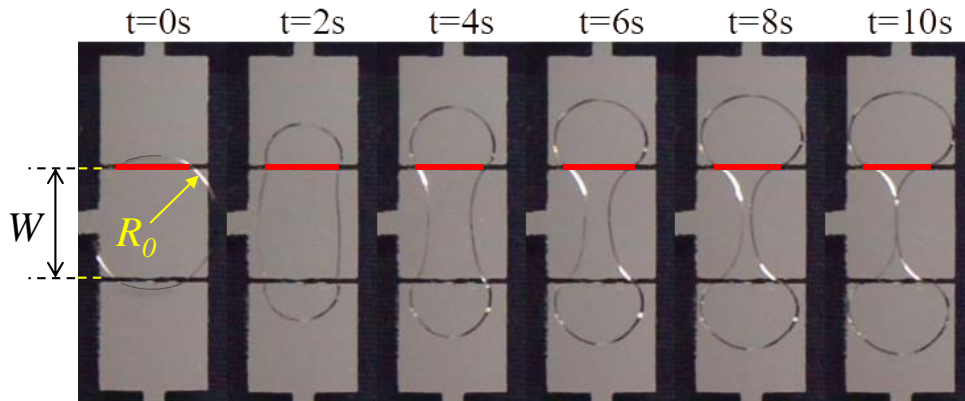


Figure 7 Images showing the droplet splitting process by EWOD ( $V_0 = 75$  V). (Red line indicates the line connecting the two intersections between the contact line and the positive and negative electrode boundaries)



In deriving Eq. (11),  $\dot{\alpha} = -\frac{\dot{R}}{R} \tan \alpha$ , from Eq. (10), was used. Since the position of the droplet front edge is given by  $L=R(1-\cos\alpha)$ , the following equation can be used to calculate the elongation rate of the droplet.

$$\dot{L} = \frac{\sin \alpha \cos \alpha - \sin \alpha}{\alpha \cos \alpha - \sin \alpha} U. \quad (12)$$

For the quadratic curve on the cathode side, the origin O is taken as the center of the axes, as shown in Fig. 8. Moreover, the  $x$ -axis is taken in the upward direction, and the  $y$ -axis is in the lateral direction. The quadratic profile of the contact line ( $y \geq 0$ ) is given by the following equation:

$$y = \left(\frac{w}{2} - a\right) \left(\frac{x}{W/2}\right)^2 + a, \quad (13)$$

where  $a$  is the half-width of the droplet contact line at the center line. From the above equation, the droplet area  $S_N$  on the negative electrode shown in Fig. 8 is obtained as follows:

$$S_N = 2 \int_0^{W/2} \left[ \left(\frac{w}{2} - a\right) \left(\frac{x}{W/2}\right)^2 + a \right] dx = W \left( \frac{2}{3} a + \frac{w}{6} \right). \quad (14)$$

From the volume conservation for a droplet, that is,  $\frac{\pi R_0^2}{2} = S_p + S_N$ , the following relationship holds for  $a$ .

$$a = \frac{1}{W} \left[ \frac{3\pi R_0^2}{4} - \frac{3w^2}{8\sin^2 \alpha} (\alpha - \sin \alpha \cos \alpha) \right] - \frac{w}{4} \quad (15)$$

Similarly, when considering the relation for volumetric flow rate as:

$$-S_N^g = U w,$$

the following equation can be used.

$$\left| \frac{\dot{a}}{a} \right| = \frac{3w}{2W} U. \quad (16)$$

Using the above relations, we considered the dynamics of the droplet, as shown in Fig. 8. The surface tension acting on the circumference of the contact line and acting on A and A' shown in Fig. 8 from the lower part of the droplet should be estimated. In addition, we should consider the pressure acting on the center cross section AA', the viscous force and inertial force. The  $x$  components of each force are evaluated as follows. In the discussion below, several approximations will be made for complicated non-linear terms to make the analysis as simple as possible.

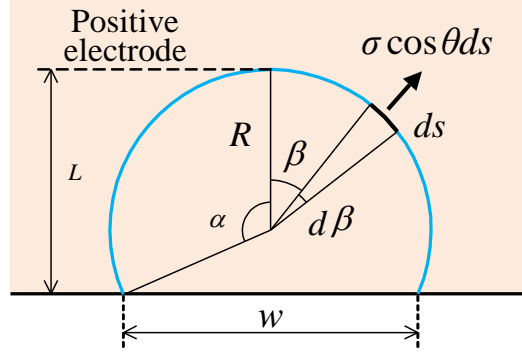


Figure 9 Surface tension  $f_s$  acting on the line element  $ds$  of the contact line on the positive electrode.

First, the resultant of the surface tension acting on the contact line was determined. Figure 9 shows the contact line on the positive electrode. The resultant force of the surface tension was estimated using the integral of the surface tension  $\sigma \cos \theta ds$  normal to the line element  $ds$  of the contact line.  $\theta$  represents the local contact angle. Since the contact line extends outward, the advancing contact angle appears in the positive electrode. Equation (8) is used to obtain the change in the contact angle  $\theta$ , depending on the velocity of the expanding contact line. Considering that the effect of the EWOD expressed by Eq. (1) only appears on the positive electrode of the lower plate, the following relations can be used to obtain the cosine of the advancing contact angles  $\theta_{LA}$  and  $\theta_{UA}$  on the lower and upper wall surfaces, respectively.

$$\cos \theta_{LA} = \cos \theta_A + \frac{CV^2}{2\sigma} - \frac{k \sin \theta_A}{3 \theta_A^2} \frac{\mu v_n}{\sigma} \quad (17)$$

$$\cos \theta_{UA} = \cos \theta_A - \frac{k \sin \theta_A}{3 \theta_A^2} \frac{\mu v_n}{\sigma}. \quad (18)$$

The second term on the right-hand side of Eq. (17) shows the change in the static contact angle due to the EWOD expressed by Eq. (1). The quasi-static advancing contact angle  $\theta_A$  was used here instead of the  $\theta_0$  used in Eq. (1). In Eqs. (17) and (18),  $v_n$  is the velocity of the contact line in the normal direction of the arc. As shown in Fig. 9, the normal velocity  $v_n$ , at the azimuthal angle  $\beta$  from the top of the contact line, can be approximated using:

$$v_n \approx \dot{L} \cos \beta \quad (19)$$

where  $\dot{L}$  is evaluated from Eq. (12). The resultant force  $F_{SP}$  of the surface tension in the longitudinal  $x$  direction acting on the circumference of the contact line shown in Fig. 9 can be evaluated as follows:

$$\begin{aligned}
F_{SP} &= 2 \int_0^\alpha \sigma \left[ \cos \theta_A + \frac{CV^2}{2\sigma} - \frac{k \sin \theta_A}{3 \theta_A^2} \frac{\mu \dot{L} \cos \beta}{\sigma} \right] R \cos \beta d\beta \\
&\quad \text{Lower wall} \\
&+ 2 \int_0^\alpha \sigma \left[ \cos \theta_A - \frac{k \sin \theta_A}{3 \theta_A^2} \frac{\mu \dot{L} \cos \beta}{\sigma} \right] R \cos \beta d\beta \\
&\quad \text{Upper wall} \\
&= \sigma w \left[ 2 \cos \theta_A + \frac{CV^2}{2\sigma} - \frac{k \sin \theta_A}{3 \theta_A^2} \frac{\mu U}{\sigma} \left( \frac{\sin \alpha \cos \alpha - \sin \alpha}{\alpha \cos \alpha - \sin \alpha} \right) \frac{\left( \alpha + \frac{1}{2} \sin 2\alpha \right)}{\sin \alpha} \right] \\
&\approx \sigma w \left[ 2 \cos \theta_A + \frac{CV^2}{2\sigma} - \frac{2k \sin \theta_A}{3 \theta_A^2} \frac{\mu U}{\sigma} \right] \tag{20}
\end{aligned}$$

In the above equation, the following approximation was made to facilitate further analysis.

$$\left( \frac{\sin \alpha \cos \alpha - \sin \alpha}{\alpha \cos \alpha - \sin \alpha} \right) \frac{\left( \alpha + \frac{1}{2} \sin 2\alpha \right)}{\sin \alpha} \approx 2$$

In the splitting process in which  $\alpha$  shown in Fig. 9 approximately varies from  $30^\circ$  to  $130^\circ$ , the mean value of the above parameter is almost equal to 2. The influence of the above approximation on the total surface tension shown below was less than 2%, since the contribution of the dynamic wetting to the total surface tension is at most 30%.

As shown in Fig. 10, the resultant force  $F_{SN}$  of the surface tension acting on the contact line of the negative electrode can be evaluated in the same manner. Since the contact line contracts inward, the receding contact angle should be used to estimate the resultant of the surface tension.  $F_{SN}$  can be evaluated as follows by using Eq. (8).

$$F_{SN} = -2W\sigma \int_0^1 \left[ \cos \theta_R - \frac{k \sin \theta_R}{3 \theta_R^2} \frac{\mu v_n}{\sigma} \right] \sin \gamma \frac{d\bar{x}}{\cos \gamma} \tag{21}$$

The relationships  $ds = \frac{dx}{\cos \gamma}$  and  $\bar{x} \equiv \frac{2x}{W}$  were used to obtain the equation above. While deriving the

above equation, note that there was a total of four contact lines on both the upper and lower walls, on both sides of  $x$  axis shown in Fig. 8. Here, the normal velocity  $v_n$  of the contact-line element was

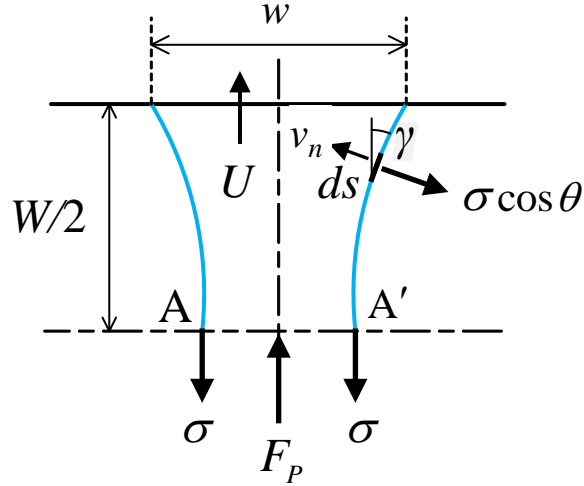


Figure 10 Schematic of the quadratic contact line on the cathode.

determined using Eq. (13) to obtain the quadratic shape of the contact line as shown below.

$$v_n = -\dot{y} \cos \gamma = -\left| \dot{a} \right| \left( 1 - \bar{x}^2 \right) \cos \gamma = -\frac{3w}{2W} U \left( 1 - \bar{x}^2 \right) \cos \gamma \quad (22)$$

In the above equation, Eq. (16) was used to determine the relation between  $\left| \dot{a} \right|$  and  $U$ . If we use the

relations,  $\cos \gamma = \frac{1}{\sqrt{1 + (dy/dx)^2}}$  and  $\sin \gamma = \frac{dy/dx}{\sqrt{1 + (dy/dx)^2}}$ , in Eq. (21),  $F_{SN}$  can be obtained as

follows:

$$\begin{aligned} F_{SN} &= -2(w - 2a)\sigma \cos \theta_R - \mu U w k \frac{\sin \theta_R}{\theta_R^2} \left[ \frac{1}{c} \left\{ \sqrt{1 + c^2} - 1 \right\} - \frac{1}{3c^3} \left\{ (1 + c^2)^{3/2} - 3\sqrt{1 + c^2} + 2 \right\} \right] \\ &\approx -2(w - 2a)\sigma \cos \theta_R - \frac{w - 2a}{2W} \mu U w k \frac{\sin \theta_R}{\theta_R^2} \quad \left[ c \equiv \frac{w - 2a}{W/2} \right] \end{aligned} \quad (23)$$

In the derivation of Eq. (23), the following relation for  $c$  obtained from the Taylor expansion was used.

$$\frac{1}{c} \left\{ \sqrt{1 + c^2} - 1 \right\} - \frac{1}{3c^3} \left\{ (1 + c^2)^{3/2} - 3\sqrt{1 + c^2} + 2 \right\} \approx \frac{1}{4} c = \frac{w - 2a}{2W}$$

The error with respect to the total surface tension ( $F_{SP} + F_{SN}$ ) calculated from Eqs. (20) and (23) when using this approximation was approximately 3%.

The surface tension acts at A and A' on the center line ( $x=0$ ) from the lower part of the droplet, as

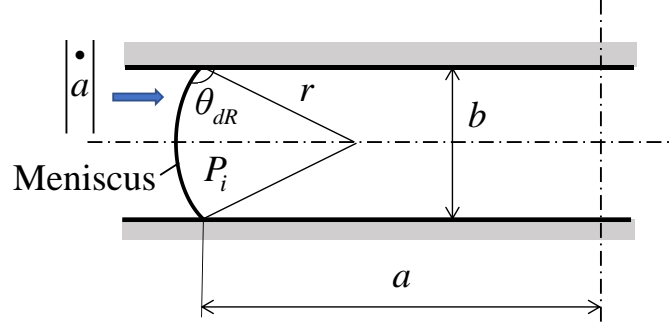


Figure 11 Schematic of droplet meniscus in center cross section of electrode.

shown in Fig. 10. Figure 11 shows a schematic of the center cross section of AA' perpendicular to  $xy$ -plane. Negative surface tension acts over the length of the meniscus appearing at the end of the droplet. For simplicity, the meniscus shape was approximated by an arc. The radius  $r$  and the length  $l_m$  of the meniscus in Fig. 11 were given by

$$r = -\frac{b}{2 \cos \theta_{dR}}, \quad l_m = r(2\theta_{dR} - \pi) = -\frac{2\theta_{dR} - \pi}{2 \cos \theta_{dR}} b. \quad (24)$$

where  $\theta_{dR}$  is the dynamic receding contact angle estimated from Eq. (8) as:

$$\cos \theta_{dR} = \cos \theta_R + \frac{1}{3} k \frac{\sin \theta_R}{\theta_R^2} \frac{\mu}{\sigma} \left| \frac{\bullet}{a} \right|.$$

Note that the contact line recedes toward the electrode center at a velocity of  $\left| \frac{\bullet}{a} \right|$ . The resultant force  $F_{SC}$  of the surface tension in the  $x$  direction, acting on the arc length of  $2 l_m$  at both ends of the central cross section, can be obtained from the following equation,

$$F_{SC} = \frac{\sigma b(2\theta_{dR} - \pi)}{\cos \theta_{dR}} \approx \frac{\sigma b(2\theta_R - \pi)}{\cos \theta_R}. \quad (25)$$

In the above equation,  $\frac{(2\theta_{dR} - \pi)}{\cos \theta_{dR}}$  was approximated by using  $\theta_R$ , since it is almost equal to -2, unless  $\theta_R$  and  $\theta_{dR}$  is not far from  $\pi/2$ . In this experiment,  $\theta_{dR}$  decreases by at most  $20^\circ$  from  $\theta_R$ . In this case, the error caused from the above approximation is within few percent.

Next, we considered the liquid pressure in the cross-section of the center line of the negative electrode. Because the effect of inertia on this phenomenon is trivial as will be shown later, the pressure  $P_i$  inside the meniscus shown in Fig. 11 is estimated using Yong-Laplace equation. By using the dynamic contact angle from Eq. (8), the following equation is obtained for the liquid pressure.

$$P_i = \frac{\sigma}{r} = -\frac{2\sigma}{b} \left[ \cos \theta_R + \frac{1}{3} k \frac{\sin \theta_R}{\theta_R^2} \frac{\mu}{\sigma} \left| \frac{\bullet}{a} \right| \right] \quad (26)$$

The difference in the pressure between that expressed in Eq. (26) and that at the electrode center was estimated by considering the balance between the pressure and the viscous drag on the wall. Here, the time scale  $t_b$ , at which the velocity boundary layer develops up to the channel center of  $b/2$  from the wall, can be evaluated using the following relation.

$$4\sqrt{\nu t_b} \sim \frac{b}{2}, \quad \therefore t_b \sim \frac{b^2}{64\nu}.$$

Assuming that the kinematic viscosity of the glycerol solution was  $\nu \sim 4.8 \times 10^{-5}$  (m<sup>2</sup>/s), and  $b = 0.53$  mm,  $t_b$  was approximately 0.1 ms using the above equation. On the other hand, the time scale  $T$  of droplet splitting, was  $\sim 10$  s in this experiment. Since  $T \gg t_b$ , the flow inside the droplet can be assumed to follow the developed two-dimensional Poiseuille flow. The  $y$ -directional velocity  $v(z)$  over the gap  $b$  can be expressed as shown below, where  $z$  is the coordinate perpendicular to the wall.

$$v = 6 \left| \frac{\bullet}{a} \right| \left[ \left( \frac{z}{b} \right) - \left( \frac{z}{b} \right)^2 \right] = 9 \frac{w}{W} U \left[ \left( \frac{z}{b} \right) - \left( \frac{z}{b} \right)^2 \right] \quad (27)$$

Note that the flow rate is  $b \left| \frac{\bullet}{a} \right|$  from the above equation. The pressure difference  $\Delta P$  between the droplet end and the electrode center can be estimated using the balance with the viscous force on the wall.

$$\Delta P = -\frac{18aw\mu U}{b^2W} \quad (28)$$

We considered a linear pressure distribution in the  $y$ -direction from  $P_i$  in Eq. (26) to  $(P_i + \Delta P)$  at the electrode center. For simplicity, we assumed that the cross-sectional area of the droplet at the center axis is  $2ba$ . Then the force  $F_P$  due to the pressure can be obtained from Eqs. (26) and (28) as follows:

$$F_P = 2ba \left[ P_i + \frac{\Delta P}{2} \right] = -4\sigma a \left[ \cos \theta_R + \frac{1}{2} k \frac{\sin \theta_R}{\theta_R^2} \frac{\mu U}{\sigma} \frac{w}{W} \right] - \frac{18a^2 w \mu U}{bW}. \quad (29)$$

Here, the resultant force of the surface tension  $F_{SP}$ ,  $F_{SN}$ ,  $F_{SC}$ , and the pressure  $F_P$ , can be obtained from Eqs. (20), (23), (25), and (29) and evaluated as shown below.

$$\begin{aligned}
& F_{SP} + F_{SN} + F_{SC} + F_P = \\
& \sigma w \left[ \frac{CV^2}{2\sigma} + 2(\cos \theta_A - \cos \theta_R) \right] + \sigma b \frac{(2\theta_R - \pi)}{\cos \theta_R} - \frac{18a^2 w \mu U}{bW} \\
& - \frac{k}{3} \mu U w \left[ 2 \frac{\sin \theta_A}{\theta_A^2} + \frac{\sin \theta_R}{\theta_R^2} \left( \frac{3a}{W} + \frac{3}{2} \frac{w}{W} \right) \right]
\end{aligned} \tag{30}$$

In the above equation, the first term on the right-hand side is the difference between the driving force due to EWOD, and the surface tension drag due to contact angle hysteresis. As seen from Eq. (30), this force acts over  $w$ , the contact line width at the positive and negative electrodes<sup>30</sup>.

The viscous drag on the droplet is then obtained. As described above, the developed two-dimensional Poiseuille flow in  $x$ -direction can be considered between the plates. The  $x$ -directional velocity distribution  $u(z)$  in the positive electrode can be expressed as follows.

$$u(z) = 6U_P \left[ \frac{z}{b} - \left( \frac{z}{b} \right)^2 \right] \tag{31}$$

$U_P$  is the average velocity at each position on the positive electrode. From the above equation, the viscous force per unit area of the wall surface is given by the following equation:

$$\tau_w = 6\mu \frac{U_P}{b} \tag{32}$$

For the positive electrode, the  $U_P$  value in the above equation changes from  $U$  at the boundary between the positive and negative electrodes, to  $\dot{L} = \frac{\sin \alpha \cos \alpha - \sin \alpha}{\alpha \cos \alpha - \sin \alpha} U$  from Eq. (12) at the top of the droplet. In the range of  $\alpha$  from  $30^\circ$  to  $130^\circ$  in the splitting process as stated before, the mean value of  $\dot{L}$  is almost equal to  $U$  within a few percent error. Here, for the sake of simplicity,  $U_P \approx U$  is assumed in Eq. (32), which is used to determine the viscous force  $F_{VP}$  on the positive electrode of the upper and lower wall surfaces as follows:

$$F_{VP} = 2 \times \frac{6\mu U}{b} S_P = \frac{12\mu U}{b} \left[ \frac{\pi R_0^2}{2} - W \left( \frac{2}{3} a + \frac{w}{6} \right) \right] \tag{33}$$

Using Eq. (14), the positive electrode area,  $S_P = \frac{\pi R_0^2}{2} - S_N$  was used in the above equation. Next, we consider the viscous force on the cathode surface. The volume reduction rate of the droplet from the origin to a certain position  $x$  should be equal to the flow rate passing through the cross section at  $x$ .

Therefore, the following equation holds for the average flow velocity  $U_N(x)$ , by using Eq. (13) for the droplet width at  $x$ .

$$-\frac{d}{dt} \int_0^x \left[ \left( \frac{w}{2} - a \right) \left( \frac{2x}{W} \right)^2 + a \right] dx = U_N(x) \left[ \left( \frac{w}{2} - a \right) \left( \frac{2x}{W} \right)^2 + a \right] \quad (34)$$

$$\therefore U_N(x) = -\frac{w}{4} \frac{\left( x^{-3} - 3x \right)}{\left( \frac{w}{2} - a \right) x^2 + a} U \quad \left[ x \equiv \frac{2x}{W} \right]$$

Here,  $\left| \frac{\bullet}{a} \right| = \frac{3w}{2W} U$ , from Eq. (16) was used. Using  $U_N(x)$  from above and assuming the wall shear stress similar to Eq. (32), the viscous force  $F_{VN}$  acting on the cathode can be calculated using the following equation.

$$F_{VN} = 4 \times 6\mu \frac{1}{b} \int_0^{w/2} U_N \left[ \left( \frac{w}{2} - a \right) \left( \frac{x}{W/2} \right)^2 + a \right] dx$$

$$= -3 \frac{\mu w W U}{b} \int_0^1 \frac{\left( x^{-3} - 3x \right)}{\left( \frac{w}{2} - a \right) x^2 + a} \left[ \left( \frac{w}{2} - a \right) x^2 + a \right] d\bar{x} = \frac{15\mu w W U}{4b} \quad (35)$$

The viscous drag  $F_V$  acting on the entire droplet can be obtained from the sum of Eqs. (33) and (35) as

$$F_V = \frac{12\mu U}{b} \left[ \frac{\pi R_0^2}{2} - W \left( \frac{2a}{3} + \frac{w}{6} \right) \right] + \frac{15\mu w W U}{4b} \quad (36)$$

Finally, the order magnitude of the inertial force of the droplet  $F_M$  can be estimated using the following equation

$$F_M \sim \frac{\rho \pi R_0^2 b}{2} \frac{dU}{dt} \sim \frac{\rho \pi R_0^2 b}{2} \frac{U}{(W/U)} = \frac{\rho \pi R_0^2 U^2}{2} \frac{b}{W}.$$

The ratio of the inertial force to the viscous force is

$$\frac{F_M}{F_V} \sim \frac{\frac{\rho \pi R_0^2 U^2 b}{2W}}{\frac{6\mu U}{b} \pi R_0^2} = \frac{\rho U b}{12\mu W} \frac{b}{W}. \quad (37)$$

Under the experimental conditions,  $\text{Re} \equiv \frac{\rho Ub}{\mu} \ll O(1)$  and  $b \ll W$ , we can conclude that

$$\frac{F_M}{F_V} \ll 1. \quad (38)$$

Hence, the inertial force can be neglected.

By equalizing Eqs. (30) and (36), the equation of motion during the droplet splitting process can be expressed as shown below.

$$\begin{aligned} & \sigma w \left[ \frac{CV^2}{2\sigma} + 2(\cos \theta_A - \cos \theta_R) \right] + \sigma b \frac{(2\theta_R - \pi)}{\cos \theta_R} - \frac{18a^2 w \mu U}{bW} - \frac{k}{3} \mu U w \left[ 2 \frac{\sin \theta_A}{\theta_A^2} + \frac{\sin \theta_R}{\theta_R^2} \left( \frac{3a}{W} + \frac{3}{2} \frac{w}{W} \right) \right] \\ & = \frac{12\mu U}{b} \left[ \frac{\pi R_0^2}{2} - W \left( \frac{2a}{3} + \frac{w}{6} \right) \right] + \frac{15\mu w W U}{4b} \end{aligned} \quad (39)$$

In Eq. (39), the first term on the left-hand side represents the difference between the driving force due to EWOD, and the drag due to contact angle hysteresis as mentioned before; and the second term is the surface tension drag acting on the center cross section. The third and fourth terms on the left-hand side represent the pressure on the center cross-section, and the drag resulting from dynamic wetting, respectively. The resultant of each force on the left-hand side is balanced with the viscous drag on the right-hand side of Eq. (39).

For the voltage  $V$  used in Eq. (39),  $V = V_0 \left( 1 - f \frac{S_P}{S} \right)$ , described in Eq. (4), should be used. Using the whole droplet adhesion area,  $S = \frac{\pi R_0^2}{2}$ , and the area on the positive electrode,  $S_P = \frac{\pi R_0^2}{2} - W \left( \frac{2a}{3} + \frac{w}{6} \right)$ , the voltage on the positive electrode is given by the following equation

$$\begin{aligned} V & = V_0 \left[ 1 - f \left\{ 1 - \frac{W(w + 4a)}{3\pi R_0^2} \right\} \right] \\ \therefore V^2 & \approx V_0^2 \left[ 1 - 2f \left( 1 - \frac{Ww}{3\pi R_0^2} \right) + 8f \frac{Wa}{3\pi R_0^2} \right] \end{aligned} \quad (40)$$

As described in Section II, the parameter  $f^2 \ll 1$  was used for the film thickness ratio  $f$ . Using Eq. (40)

and  $U = -\frac{2W}{3w} \dot{a}$  from Eq. (16), Eq. (39) can be rewritten as the ordinary differential equation for  $a$  as shown below.

$$\begin{aligned} & \frac{CV_0^2}{2\sigma} \left[ 1 - 2f \left( 1 - \frac{Ww}{3\pi R_0^2} \right) \right] + \frac{4CV_0^2}{\sigma} \frac{fW^2}{3\pi R_0^2} \bar{a} + 2(\cos \theta_A - \cos \theta_R) + \frac{b}{w} \frac{(2\theta_R - \pi)}{\cos \theta_R} \\ & = -\frac{2W}{3w} \dot{a} \left[ 18 \frac{W}{b} \bar{a}^{-2} + \bar{a} \left( k \frac{\sin \theta_R}{\theta_R^2} - 8 \frac{W^2}{bw} \right) + \frac{2}{3} k \frac{\sin \theta_A}{\theta_A^2} + \frac{1}{2} k \frac{w}{W} \frac{\sin \theta_R}{\theta_R^2} + \frac{6\pi R_0^2}{bw} + \frac{7}{4} \frac{W}{b} \right] \end{aligned} \quad (41)$$

where  $\bar{a} = \frac{a}{W}$  and  $\dot{\bar{a}} = \frac{\mu \dot{a}}{\sigma}$ . The equation above is rewritten by multiplying the right and left-hand sides by  $\frac{3\pi R_0^2 \sigma}{4fCV_0^2 W^2}$ , obtaining the following equation for  $\bar{a}$ .

$$\bar{a} + C_L = \left( C_{R0} + C_{R1} \bar{a} + C_{R2} \bar{a}^2 \right) \dot{\bar{a}}, \quad (42)$$

where

$$C_L = \frac{3\pi R_0^2 \sigma}{4fCV_0^2 W^2} \left[ \frac{CV_0^2}{2\sigma} \left\{ 1 - 2f \left( 1 - \frac{Ww}{3\pi R_0^2} \right) \right\} + 2(\cos \theta_A - \cos \theta_R) + \frac{b}{w} \frac{(2\theta_R - \pi)}{\cos \theta_R} \right], \quad (43)$$

$$C_{R0} = -\frac{\pi k R_0^2 \sigma}{3fCV_0^2 Ww} \frac{\sin \theta_A}{\theta_A^2} - \frac{\pi k R_0^2 \sigma}{4fCV_0^2 W^2} \frac{\sin \theta_R}{\theta_R^2} - \frac{3\pi^2 R_0^4 \sigma}{fCV_0^2 bWw^2} - \frac{7\pi R_0^2 \sigma}{8fCV_0^2 bw}, \quad (44)$$

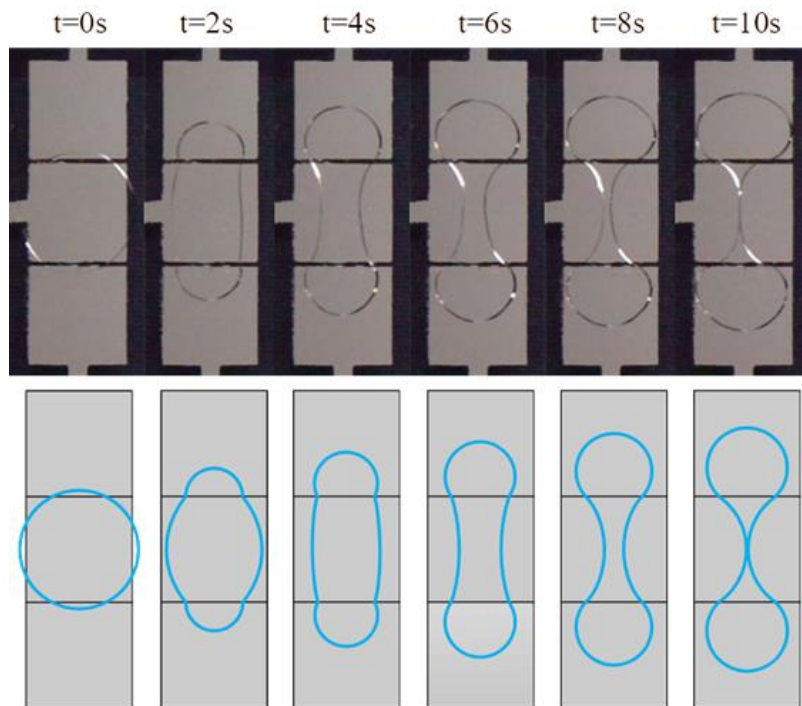
$$C_{R1} = -\frac{\pi k R_0^2 \sigma}{2fCV_0^2 Ww} \frac{\sin \theta_R}{\theta_R^2} + \frac{4\pi R_0^2 W \sigma}{fCV_0^2 bw^2}, \quad (45)$$

$$C_{R2} = -\frac{9\pi R_0^2 \sigma}{fCV_0^2 bw}. \quad (46)$$

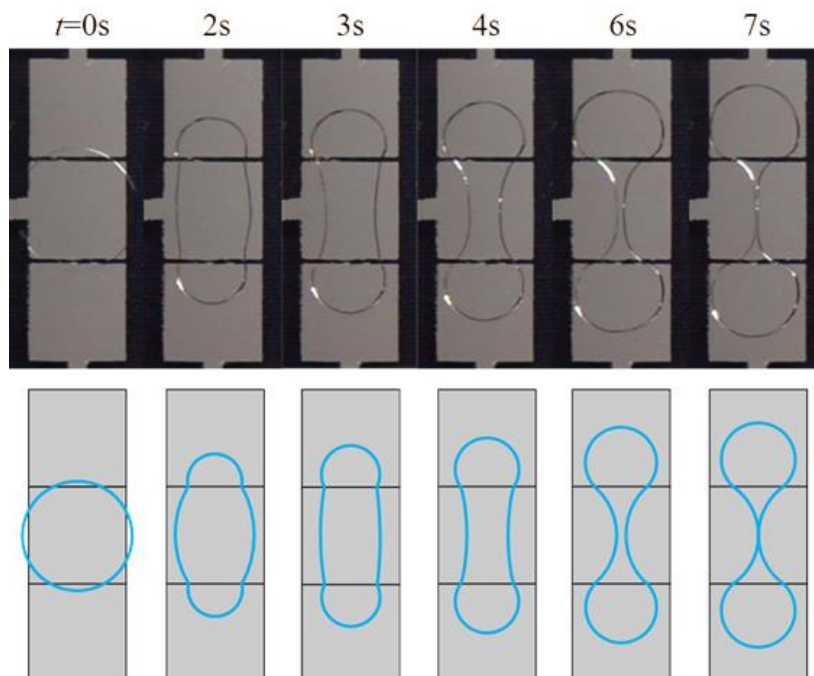
Equation (42) can be easily solved by separating the variables as

$$\bar{t} \equiv \frac{\sigma t}{\mu W} = \frac{1}{2} C_{R2} \left( \bar{a}^{-2} - \bar{a}_0^{-2} \right) + (C_{R1} - C_L C_{R2}) (\bar{a} - \bar{a}_0) + \left\{ C_{R0} - C_L (C_{R1} - C_L C_{R2}) \right\} \ln \left( \frac{\bar{a} + C_L}{\bar{a}_0 + C_L} \right) \quad (47)$$

Here,  $a_0$  represents the half-width of the droplet at  $t = 0$ . Thus, the droplet half-width  $a$  on the electrode center, and each geometric quantity related to the droplet shape, such as  $R$ ,  $\alpha$  or  $L$  in Fig. 8, can be calculated.



(a)  $V_0 = 75V$



(b)  $V_0 = 80V$

Figure 12 Comparison of the observed and calculated results for time-dependent changes in the droplet shape (Upper: continuous photo of observations, Lower: theoretical results)

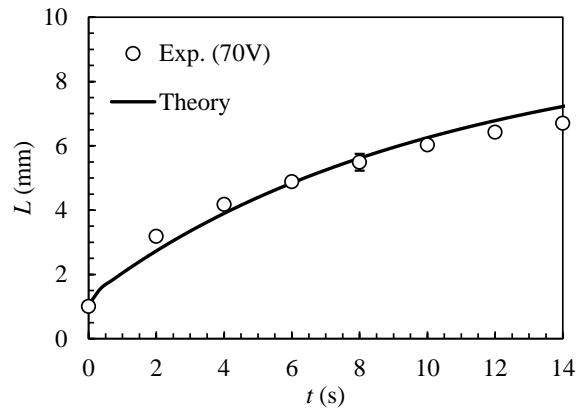
## IV. Experimental results and discussion

### A. Experimental results of the splitting process

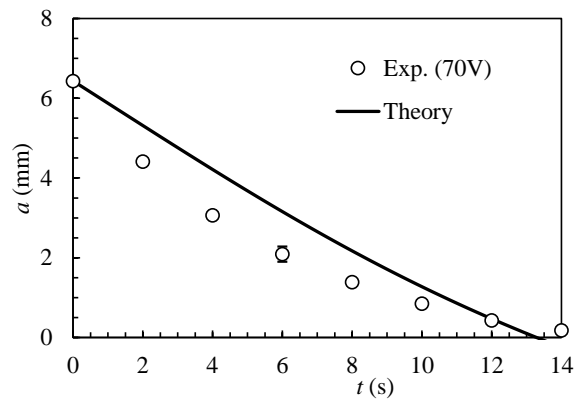
The Cytop film used in this experiment easily suffered dielectric breakdown when the voltage was higher than 80V. Considering the voltage at which the droplet is actually driven by the EWOD, which will be described later, the measurement results made in the range of 70-80V are shown below. Using the voltages  $V_0 = 75$  V and 80 V, the droplet shape at each time was calculated using Eq. (47), and Figure 12 shows a comparison with the observed droplet shape until final splitting occurs. The initial droplet radius is set to approximately 6 mm, as shown in Figs. 12 (a) and (b). The upper part of each figure shows an actual photograph, and the lower part shows the theoretical results. The inflow into the positive electrode started after the voltage was applied, resulting in an increase in the adhesion area on the positive electrode. On the other hand, as the volume in the cathode decreased, the width of the contact line at the center also decreased, until the droplet split into two. The time of splitting was 11.5 s and 7.8 s for 75 V and 80 V, respectively. The splitting time changed more than 30 %, even with a small voltage difference. From Eq. (41), we obtained the lower limit of the voltage  $V_0$  at which the droplet can be driven by the EWOD. When the velocity  $\dot{a}$  on the right-hand side of Eq. (41) is zero, the lower limit  $V_0$  can be obtained from the condition that the sum on the left-hand side is zero. The calculated result of  $V_0 \approx 58$  V is comparable with the experimentally observed  $V_0 \approx 60$  V, above which the droplet was actually driven by EWOD. Because the difference in the voltage from this lower limit corresponds to the actual driving force, a noticeable distinction is noted in the splitting time between  $V_0 = 75$  V and 80 V. As shown in Fig. 12, the theoretical model proposed in this study can reproduce the time-dependent changes in the droplet shape.

Figure 13 shows the time change of the droplet length  $L$  on the positive electrode, and the half width  $a$  at the cathode center, for  $V_0 = 70$ V. Each plot represents an average of five measurements. It can be seen that the theoretical model can adequately approximate the experimental results for the length  $L$ . However, for  $a$ , the theoretical results are slightly larger than the experimental measurements at each time until the final split. This may be due to the fact that the contact line shape is approximated by a simple parabolic. In addition, the width  $w$  of the contact line at the electrode boundary was assumed to be constant in the theoretical model. However, it was observed that  $w$  increased slightly from the initial width, by approximately 10%, and then remained almost constant. In Eq. (39), the first term on the left-hand side represents the driving force by EWOD. Since the actual driving force increases slightly as  $w$  increases, the droplet width contracts faster than that in the theoretical model. For other experimental conditions, the theoretical and experimental results were similar to those shown in Fig.13.

Figure 14 shows the time  $T$  when droplet splitting occurs. Note that another substrate ( $C = 1.60 \times 10^{-5}$  F/m<sup>2</sup>,  $f = 0.108$ ) was also used to measure the split time. As shown in the figure, the experimental



(a) Droplet length on the positive electrode



(b) Half width of the droplet at the electrode center

Figure 13 Relationship between the time change and geometrical length ( $V_0 = 70V$ ).

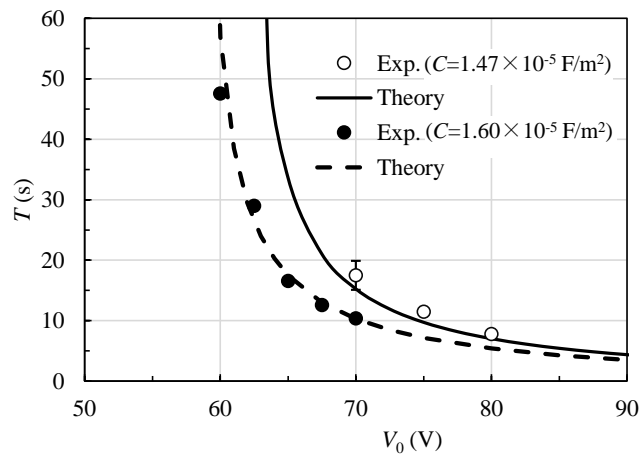


Figure 14 Change in the split time with the applied voltage.

results of  $T$  can be approximated using the model proposed in this study. In the actual experiment, the half-width at the electrode center continuously decreased up to approximately 1 mm. However, it took

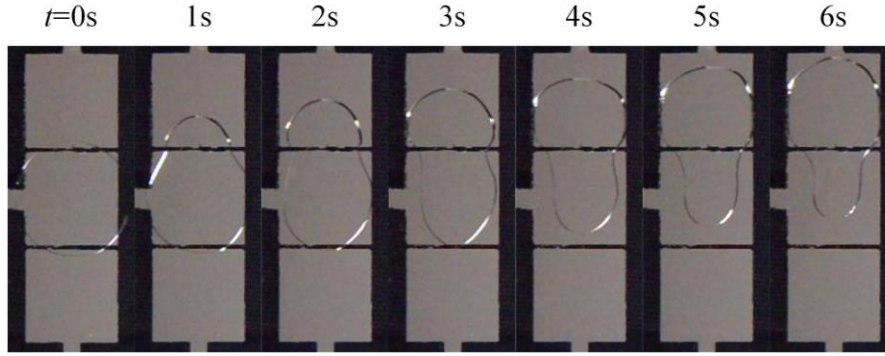


Figure 15 Successive images of droplet movement in one direction ( $V_0 = 80$  V).

some time to reach the final split. In the theoretical model of this study, the physics behind the thread breaking of the final stage was not considered, allowing the underestimation of the splitting time  $T$ . On the other hand, as mentioned above,  $w$  increases slightly in the actual phenomenon, so the contraction proceeds faster. As a result of these canceling effects, the theoretical model can reproduce well the actual splitting time.

## B. Behavior of contact line width at positive and negative electrode boundaries

In Section III, the theoretical analysis was performed assuming that the contact line width  $w$  at the boundary between positive and negative electrodes was constant. Figure 15 shows an example of successive images taken when there is only one positive electrode, with the droplet simply moving from the negative to the positive electrode without splitting. Compared to Fig. 12 (b) at the same voltage, it was observed that  $w$  increases remarkably during droplet movement. We considered such a difference of droplet behavior as well as the validity of the assumption in Section III, based on an approximate theoretical model.

Figures 16 (a) and (b) show a schematic of the contact lines for splitting and simple movement. Droplet deformation can be assessed using the principle of minimum work by first considering the case where the droplet splits, as shown in Fig. 16(a). Figure 17 shows an enlarged schematic of the contact line. Because the contact line is symmetric, the upper half is taken as the target system. We compared the contact line of the initial arc with a radius  $R_0$ , denoted by the dotted line in Fig. 17 with that of the solid line after a part of the liquid has moved to the positive electrode side. An assumption was made that  $w$  increases from the initial  $w_0$ . The energy in the system changed during deformation. The increase in the surface energy was due to the change in the liquid surface area (meniscus area as shown in Fig. 11) because of the deformation of the contact line, and the work due to wetting behavior where the negative electrode is dried while the positive electrode is wetted. In addition, for the negative electrode

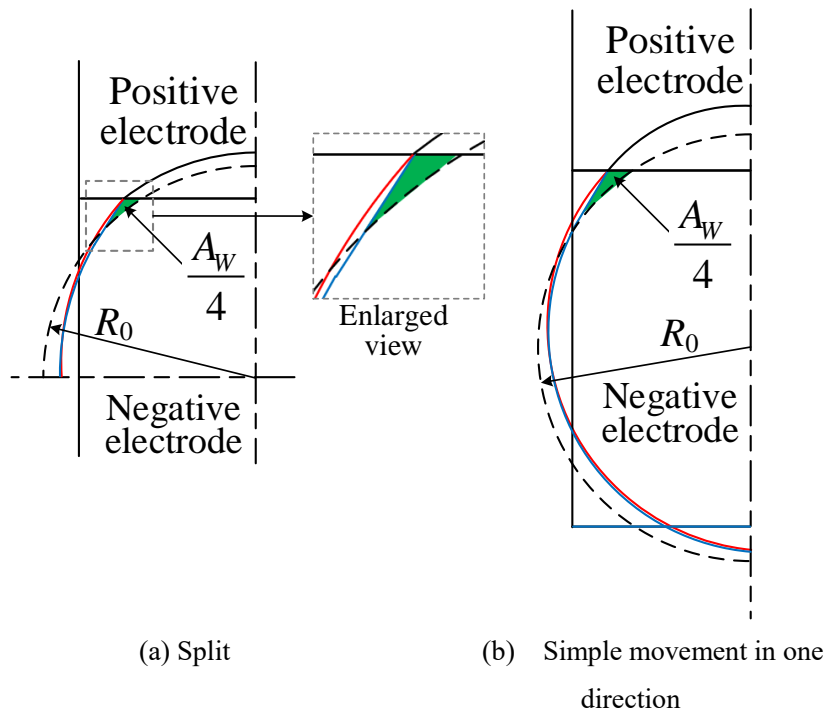


Figure 16 Deformation of the droplet contact line due to an increase in the contact line width at electrodes boundary (red contact line is an arc and blue contact line is combination of a straight line and an arc in cathode).

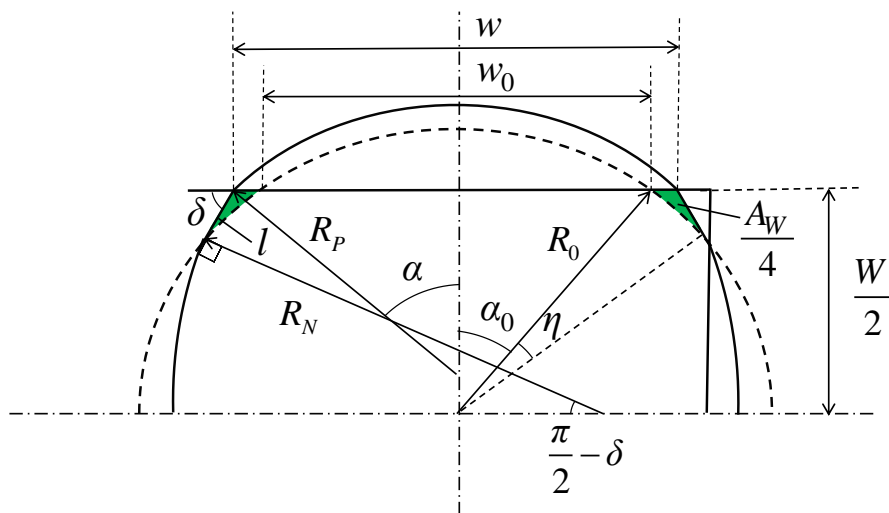


Figure 17 Shape of the contact line during splitting.

when the width  $w$  was increased, a certain area was newly wetted (green area in Fig. 17). The total of newly wetted area was expressed as  $A_W$ . When the total adhesion areas of the upper and lower wall surfaces of the positive electrodes is  $A_P$ , the energy change in the system, from the initial circular contact line, is considered.

The energy change per unit area  $e_A$  ( $e_R$ ) when wetting (drying) a solid surface can be obtained from

the following relation using modified Young's equation for the contact angle<sup>5,32</sup>.

$$e_A = -\sigma \cos \theta_A \quad (48)$$

$$e_R = \sigma \cos \theta_R \quad (49)$$

By multiplying Eqs. (48) and (49) by the actual wetted (dried) area, the work due to wetting can be evaluated. The energy change on the liquid surface can be calculated by multiplying the surface tension  $\sigma$  by the increase in the liquid surface area. The perimeter lengths of the contact line drawn by the solid line on the positive and negative electrodes are represented by  $L_P$  and  $L_N$ , respectively. The energy change  $E$  of the system can be obtained using the following equation.

$$\begin{aligned} E &= \sigma \left[ b(L_P + L_N) - \pi b R_0 \right] - \sigma \cos \theta_A \left[ A_P + A_W - A_{P0} \right] + \sigma \cos \theta_R \left[ A_P + A_W - A_{P0} \right] - \frac{CV^2}{2} \left[ \frac{A_P}{2} - \frac{A_{P0}}{2} \right] \\ &= \sigma b (L_P + L_N - \pi R_0) + \sigma (\cos \theta_R - \cos \theta_A) \left[ A_P + A_W - 2R_0^2 (\alpha_0 - \sin \alpha_0 \cos \alpha_0) \right] \\ &\quad - \frac{CV^2}{2} \left[ \frac{A_P}{2} - R_0^2 (\alpha_0 - \sin \alpha_0 \cos \alpha_0) \right] \end{aligned} \quad (50)$$

Here,  $A_{P0}$  is the initial area of the positive electrode. The following relation was used to estimate  $A_{P0}$ .

$$A_{P0} = 2R_0^2 (\alpha_0 - \sin \alpha_0 \cos \alpha_0) \quad (51)$$

$\alpha_0 \left( = \sin^{-1} \frac{w_0}{2R_0} \right)$  is the half central angle of the arc as shown in Fig. 17. In Eq. (50), the first term on the right-hand side in the first line represents the energy change corresponding to the increase in the liquid surface area. The meniscus length  $l_m$  from Eq. (24) can be evaluated from the following equation using  $\frac{(\pi/2 - \theta_R)}{\cos \theta_R} \approx 1$ , when  $\theta_R$  is not far from  $\pi/2$ .

$$l_m = \frac{b(\pi/2 - \theta_R)}{\cos \theta_R} \approx b \quad (52)$$

Using Eq. (52), the surface area of the liquid meniscus between the upper and lower plates is represented by  $b(L_P + L_N)$  in Eq. (50). The error in the total energy  $E$  for this approximation is less than 2%. The second and third terms represents the work due to wetting behavior. Note that the actually wetted (dried) area can be expressed by  $(A_P + A_W - A_{P0})$ . The last term on the right-hand side of Eq. (50) represents the energy reduction due to EWOD. It is noted that the effect of EWOD appears on the lower surface only,

although the droplet wets both the upper and lower surfaces.

As the contact line width at the two electrodes boundary increases, the wetted area  $A_W$ , drawn by green area in Figs. 16 and 17, is formed as stated above. Since the same area is dried extra in addition to  $(A_P - A_{P0})$ , an increase in the width results in excess work, corresponding to the difference between Eqs. (48) and (49). This effect is represented in the term multiplied by  $\sigma(\cos\theta_R - \cos\theta_A)$  in Eq. (50). If the width is kept constant, there will be no work corresponding to  $A_W$ . On the contrary, the energy of the liquid surface area increases since the contact line is distorted more remarkably and the length of contact line increases. The droplet should be deformed in such a way that the sum of the two kinds of energy changes is minimized. It should be noted that if the width decreases from that at the initial state, excess work is required to dry the surface of the positive electrode near the electrode boundary, and the distortion of the contact line from the initial arc becomes larger than that observed when  $w$  increases. Therefore, the case of width reduction is not considered here.

The solid red line in Fig. 16 shows the circular contact line on the cathode. The solid blue line is a combination of a straight line and a circular arc smoothly connected to it. The straight line crosses the initial circular contact line with a certain inclination from the positive and negative electrode boundary lines. As can be seen from the enlarged view in Fig. 16 (a), when the contact line on the cathode is represented by a simple arc or a polynomial, the intersection with the initial contact line shifts to a considerably lower position, and the  $A_W$  becomes larger. Assuming an arc-shaped contact line, shown by the red line in Fig. 16 (a), it can be confirmed that  $E$  in Eq. (50) is minimized when the contact line width  $w$  at the boundary between positive and negative electrodes does not change from that of the initial arc. As a virtual contact line that makes  $A_W$  as small as possible, shown in Fig. 17, the contact line on the cathode is approximated using a combination of straight line with a length  $l$  and an inclination  $\delta$ , and arc radius of  $R_N$ . Each geometrical parameter ( $\delta$ ,  $l$ , and  $R_N$ ) is determined in such a way that  $E$  is minimized, while also satisfying the geometric constraints. Actually, the contact line approximated by the straight line and arc stated above may not be exact. In principle, the curve of the contact line that minimizes Eq. (50) should be calculated from the variational principle. However, if we can find a width at which the system energy is smaller than that at  $w_0$  by using the assumed contact line, the droplet can be deformed with increasing the contact line width, because the energy for the actual contact line should become smaller.

The width corresponding to the minimum  $E$  described in Eq. (50) was calculated when the wetted area on the positive electrode reached a certain value of  $A_P$ . Although each related value can be obtained from simple geometry, the calculation is somewhat troublesome. Here the calculation procedure is briefly described below. The total circumference of the contact line ( $L_P + L_N$ ) on the positive and negative electrodes in Eq. (50) can be calculated as follows.

$$L_P + L_N = 2 \left[ R_P \alpha + l + R_N \left( \frac{\pi}{2} - \delta \right) \right] \quad (53)$$

$R_P$  is the radius of the arc on the positive electrode, as shown in Fig. 17, and  $\alpha$  is half the center angle of the arc. The unknown parameters  $R_P$ ,  $\alpha$ ,  $l$ ,  $R_N$  and  $\delta$  in the above equation are estimated as follows. The following equations can be used for  $R_P$ :

$$R_P = \frac{w}{2 \sin \alpha} \quad (54)$$

In addition, we can use the following relationship between the wetted area  $A_P$  on the positive electrode, and  $w$ .

$$A_P = 2R_P^2 (\alpha - \sin \alpha \cos \alpha) \quad (55)$$

If  $A_P$  and  $w$  are given,  $\alpha$  and  $R_P$  can be determined by solving the simultaneous nonlinear algebraic equations in Eqs. (54) and (55). Next, the following relation can be written for the cathode-side adhesion area, with reference to Fig. 17.

$$\begin{aligned} \pi R_0^2 - A_P &= 2R_N^2 \left( \frac{\pi}{2} - \delta - \sin \delta \cos \delta \right) + 2(w + 2l \cos \delta) R_N \cos \delta + 2(w + l \cos \delta) l \sin \delta \\ &= 2R_N^2 \left( \frac{\pi}{2} - \delta - \sin \delta \cos \delta \right) + 2l \cos \delta (2R_N \cos \delta + l \sin \delta) + 2w(R_N \cos \delta + l \sin \delta) \end{aligned} \quad (56)$$

The following relation can be used for  $R_N$ :

$$R_N = \frac{\frac{W}{2} - l \sin \delta}{\cos \delta}. \quad (57)$$

Now we introduce another parameter  $\eta$  appearing in Fig.17, that is, the center angle formed in the dotted initial arc by both ends of the  $A_W$  region. The following equations can be obtained from geometrical consideration.

$$R_0 \sin(\alpha_0 + \eta) - \frac{w}{2} = l \cos \delta \quad (58)$$

$$R_0 [\cos \alpha_0 - \cos(\alpha_0 + \eta)] = l \sin \delta \quad (59)$$

If the adhesion area  $A_P$  and width  $w$  are given, the undetermined parameters  $R_N$ ,  $\delta$ ,  $l$ , and  $\eta$  are solved using the four simultaneous nonlinear algebraic equations described by Eqs. (56) to (59). As a result,  $(L_P+L_N)$  in Eq. (53) can be calculated.

The wetted area  $A_W$  on the cathode, as shown in Figs. 16 (a) and 17, can be calculated using each

parameter mentioned above as follows.

$$A_W = 4 \left[ \frac{(w-w_0)}{4} R_0 \{ \cos \alpha_0 - \cos(\alpha_0 + \eta) \} - \frac{1}{2} R_0^2 (\eta - \sin \eta) \right] \quad (60)$$

The coefficient 4 on the right-hand side of the equation above is to account for the fact that the wetted area on the cathode is on both the upper and lower walls.

When Eqs. (53) to (60) are combined with Eq. (50), the energy change  $E$  can be expressed as follows.

$$\begin{aligned} E = \sigma b & \left[ \frac{w\alpha}{\sin \alpha} + 2l + \frac{W - 2l \sin \delta}{\cos \delta} \left( \frac{\pi}{2} - \delta \right) - \pi R_0 \right] \\ & + \sigma (\cos \theta_R - \cos \theta_A) \left[ A_P + R_0 (w - w_0) \{ \cos \alpha_0 - \cos(\alpha_0 + \eta) \} \right. \\ & \left. - 2R_0^2 (\eta - \sin \eta) - 2R_0^2 (\alpha_0 - \sin \alpha_0 \cos \alpha_0) \right] - \frac{CV^2}{2} \left[ \frac{A_P}{2} - R_0^2 (\alpha_0 - \sin \alpha_0 \cos \alpha_0) \right] \end{aligned} \quad (61)$$

For a certain  $A_P$  value,  $E$  in Eq. (61) can be expressed as a function of  $w$ . The width corresponding to the minimum energy can be obtained from the following condition:

$$\text{at } A_P: \quad \frac{dE}{dw} = 0 \quad (62)$$

When the droplet moves on the plate in one direction without splitting as shown in Fig. 18, the width that minimizes the energy can be obtained in a manner similar to that stated above. The energy change  $E$  for the droplet contact line profile, as shown in Fig. 18, is calculated as follows.

$$\begin{aligned} E = \sigma b & \left[ \frac{w\alpha}{\sin \alpha} + l + \frac{(w + 2l \cos \delta)(\pi - \delta)}{\sin \delta} - 2\pi R_0 \right] \\ & + \sigma (\cos \theta_{SR} - \cos \theta_{SA}) \left[ A_P + R_0 (w - w_0) \{ \cos \alpha_0 - \cos(\alpha_0 + \eta) \} \right. \\ & \left. - 2R_0^2 (\eta - \sin \eta) - 2R_0^2 (\alpha_0 - \sin \alpha_0 \cos \alpha_0) \right] - \frac{CV^2}{2} \left[ \frac{A_P}{2} - R_0^2 (\alpha_0 - \sin \alpha_0 \cos \alpha_0) \right] \end{aligned} \quad (63)$$

Each parameter, namely  $\alpha$ ,  $\eta$ ,  $\delta$ , and  $l$  in the above equation can be obtained from the geometrical consideration similar to that described above for droplet splitting. The energy  $E$  of Eq. (63) can be taken as a function of  $w$  for a certain value of  $A_P$ , and the width corresponding to the minimum energy can be estimated using the following relation:

$$\text{at } A_P: \quad \frac{dE}{dw} = 0 \quad (64)$$

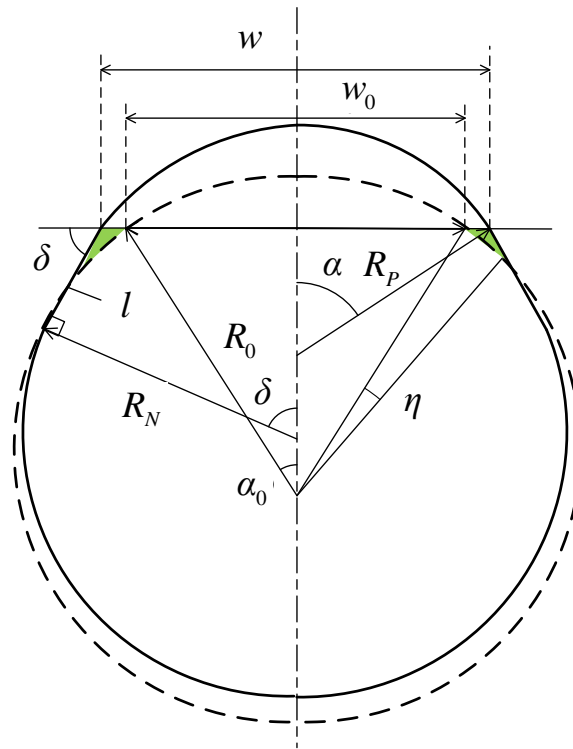


Figure 18 Shape of the contact line during droplet movement.

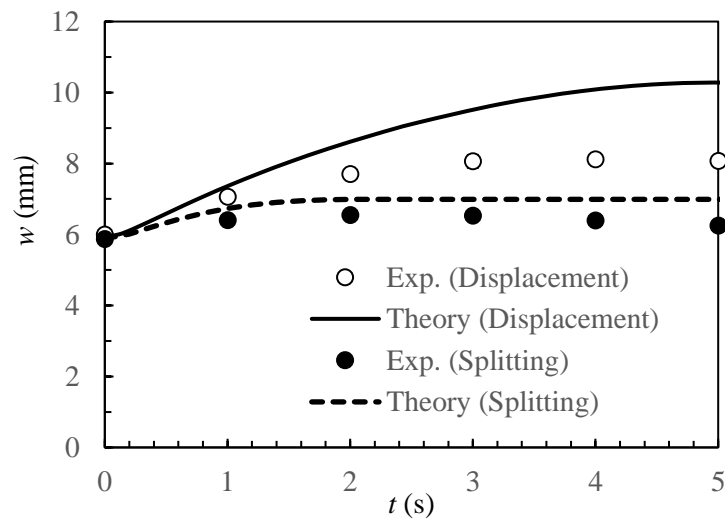


Figure 19 Time change with the contact line width  $w$  at electrodes boundary widths ( $V_0 = 80V$ ).

Figure 19 shows a comparison of the widths obtained using the model above, and the experimental results. In the experiment when the droplet simply moved in one direction, the voltage for one of the two positive electrodes was set to zero, and the movement of the droplet with an initial radius of 6 mm was observed. Figure 19 shows results for  $V_0 = 80$  V, with similar results being obtained using other voltages. The

experimental width  $w$  for the droplet splitting increased slightly from the initial value, and then remained almost constant. However, in the case of simple movement,  $w$  tends to asymptotically approach a constant value while increasing monotonically. As shown in Fig. 19, the calculated results obtained from the model above are consistent with the experimental results, despite some discrepancies. It is possible to explain the qualitative behavior of the contact line width at the electrodes boundary using the principle of minimum work, although the theoretical model used some approximations. In the case of simple movement without splitting, the theoretical width is smaller than the experimental value after  $t = 2\text{s}$ . This is thought to be because the contact line shape on the negative electrode is flatter and thinner than the arc assumed in the theoretical model, as shown in Fig. 15.

The difference in the behavior of the width during splitting or simple unidirectional movement, as shown in Fig. 19, can be understood as follows. For droplet splitting, as shown in Fig. 12, the contact line inside the cathode has a convex shape toward the outside (from  $t = 0$  to a certain time). If  $w$  increases during this time, the length of the contact line inside the cathode is reduced, and the liquid surface energy decreases. Because the volume is larger in the cathode at around  $t = 0$ , the contact line length is also relatively large. Therefore,  $w$  may increase slightly if the decrease in the liquid surface energy exceeds the work corresponding to creating the area  $A_w$  stated above. However, because the liquid in the cathode is transferred to the two positive electrodes, the volume in the cathode decreases rapidly. As can be seen in Fig. 12 (b), at  $t = 4\text{ s}$  after  $w$  in Fig. 19 is maximum, the droplet contact line on the cathode curves inwards in a concave manner. Assuming that the width increases when the contact line on the cathode has a concave shape, the length of the contact line and  $A_w$  also increases, compared to when  $w$  is constant. Therefore, since the increase in  $w$  requires more energy, the width  $w$  cannot be further increased when the contact line on the cathode has a concave shape. On the other hand, when the droplet moves in one direction, the volume of the liquid on the cathode is larger compared to that when splitting. Thus, the contact line on the cathode is maintained in a convex shape as shown in Fig. 15. Since the energy reduction due to the decrease in the contact line length is big, it is believed that a continuous increase in  $w$  is possible. The different behaviors of  $w$  may appear depending on the shape of the contact line on the cathode side.

In the case of simple movement without splitting in Fig. 19, the actual droplet width becomes smaller than the theoretical results after  $t = 2\text{s}$ . Since the contact line shape on the negative electrode becomes thinner than the arc as mentioned above, the energy is not significantly reduced with the increase in the width  $w$ . This may be the reason why  $w$  observed in the actual system does not increase as expected by the theoretical model.

## V. Conclusion

A theoretical consideration was made on the EWOD-induced splitting process of droplets placed in the Hele-Shaw cell. From the symmetry of the droplet shape, the equation of motion of the half droplet

part from the center axis was derived. The resultant force of the surface tension acting on the contact line on the electrodes, and on the meniscus in the center cross section was evaluated in consideration of the effect of dynamic wetting. In addition, the pressure acting on the center cross section and the viscous drag on the wall were estimated. The equation of motion was derived from each force balance and an analytical solution was obtained that represents the time variation of the droplet width at the center line. For the system used in this study, the effect of dynamic wetting on the movement of droplets was approximately 30%. The calculated results obtained from the theoretical model showed behavior similar to the experimentally observed movement of the droplets during the splitting process. The theoretical model suggests that the driving force behind droplet motion is proportional to the contact line width at the boundary between the positive and negative electrodes. The behavior of the contact line width was theoretically evaluated using an approximate model based on the principle of minimum work. When the droplet is pulled towards the two positive electrodes, the contact line in the cathode becomes concave. It was shown that the width is kept almost constant, such that the sum of the work related to wetting, and the energy of the liquid surface due to contact line deformation, is minimized.

## REFERENCE

1. A. A. Darhuber, and S. M. Troian, "Principles of microfluidic actuation by modulation of surface stresses." *Annual Review of Fluid Mechanics* **37**, 425-455(2005).
2. P. Abgrall and A. M. Gué, "Lab-on-chip technologies: making a microfluidic network and coupling it into a complete microsystem—a review," *Journal of Micromechanics and Microengineering*, **17**, R15–R49(2007).
3. S. Gupta, K. Ramesh, S. Ahmed and V. Kakkar, "Lab-on-chip technology: a review on design trends and future scope in biomedical applications," *International Journal of Bio-Science and Bio-Technology* **5**, 311–322(2016).
4. H. D. Xi, H. Zheng, W. Guo, A. M. Gañán-Calvo, Y. Ai, C. W. Tsao, J. Zhou, W. Li, Y. Huang, N. T. Nguyenh and S. H. Tan, "Active droplet sorting in microfluidics: a review," *Lab on a Chip*, **17**, 751–771(2017).
5. K. Katoh(加藤健司), H. Tamura(田村大樹), E. Sato(佐藤絵理子) and T. Wakimoto(脇本辰郎), "Control of droplet movement on an inclined wall with sawtoothed wettability pattern by applying ultrasonic vibration," *Experiments in Fluids* **59**, 141 (10 pages) (2018).
6. K. Katoh(加藤健司), E. Sato(佐藤絵理子), S. Yoshioka(吉岡真弥) and T. Wakimoto(脇本辰郎), "Control of droplet movement on a plate with micro-wrinkle by difference of wettability," *Experiments in Fluids* **60**, 141 (10 pages) (2019).
7. G. Lippmann, "Relations entre les phénomènes électriques et capillaires," *Annales de Chimie et de Physique*, **5**, 494-549 (1875).

8. K. H. Kang, "How Electrostatic Fields Change Contact Angle in Electrowetting," *Langmuir*, **18**, 10318-10322 (2002).
9. H. Ren, R. B. Fair, M. G. Pollack and E. J. Shaughnessy, "Dynamics of electro-wetting droplet transport," *Sensors and Actuators B* **87**, 201-206(2002).
10. S. K. Cho, H. Moon and C.-J. Kim, "Creating, transporting, cutting, and merging liquid droplets by electrowetting-based actuation for digital microfluidic circuits," *Journal of Microelectromechanical Systems*, **12**, 70-80(2003).
11. J. H. Song, R. Evans, Y.-Y. Lin, B.-N. Hsu and R. B. Fair, "A scaling model for electrowetting-on-dielectric microfluidic actuator," *Microfluidics and Nanofluidics*, **7**, 75-89(2009).
12. K. Suzuki, H. Homma, T. Murayama, S. Fukuda, H. Takanobu and H. Miura, "Electrowetting-based actuation of liquid droplets for micro transportation systems," *Journal of Advanced Mechanical Design, Systems, and Manufacturing*, **4**, 365-372(2010).
13. M. Abdelgawad, P. Park and R. Wheeler, "Optimization of device geometry in single-plate digital microfluidics," *Journal of Applied Physics* **105**, 094506(2009).
14. V. Jain, V. Devarasetty and R. Patrikar, "Effect of electrode geometry on droplet velocity in open EWOD based device for digital microfluidics applications," *Journal of Electrostatics*, **87**, 11–18(2017).
15. M. M. Nahar, J. B. Nikapitiya, S. M. You and H. Moon, "Droplet velocity in an electrowetting on dielectric digital microfluidic device," *Micromachines* **7**, 1–16(2016).
16. F. Mugele and J.-C. Baret, "Electrowetting: from basics to applications," *Journal of Physics: Condensed Matter*, **17**, R705—R774(2005).
17. F. Mugele and J. Buehrle, "Equilibrium drop surface profiles in electric fields," *Journal of Physics: Condensed Matter*, 375112-1-20 (2007).
18. M. Basu, V. P. Joshi, S. Das and S. Dasgupta, "Analysis of augmented droplet transport during electrowetting over triangular coplanar electrode array," *Journal of Electrostatics*, **109**, 103541 (11 pages)(2021).
19. R. Dey, J. Gilbers, D. Baratian, H. Hoek, D. van den Ende and F. Mugele, "Controlling shedding characteristics of condensate drops using electrowetting," *Applied Physics Letters*, **113**, 243703-1-5(2018).
20. J. Tan, P. Tian, M. Sun, H. Wang, N. Sun, G. Chen, Y. Song, D. Jiang, H. Jiang, M. Xu, "A transparent electrowetting-on-dielectric device driven by triboelectric nanogenerator for extremely fast anti-fogging," *Nano Energy*, **92**, 106697 (8 pages) (2022).
21. Y. Cheng, J. Cao, Q. Hao, "Optical beam steering using liquid-based devices," *Optics and Lasers in Engineering*, **146**, 106700 (21 pages) (2021).
22. J. M. Oh, S. H. Ko and K. H. Kang, "Shape oscillation of a drop in AC electrowetting," *Langmuir* **24**, 8379-8386(2008).

23. J. M. Oh, S. H. Ko and K. H. Kang, "Analysis of electrowetting-driven spreading of a drop in air," *Physics of Fluids* **22**, 032002-1-10(2010).
24. S. H. Ko, H. Lee and K. H. Kang, "Hydrodynamic flows in electrowetting," *Langmuir* **24**, 1094-1101(2008).
25. H.-W. Lu, K. Glasner, A. L. Bertozzi and C.-J. Kim, "A diffuse-interface model for electrowetting drops in a Hele-Shaw cell," *Journal of Fluid Mechanics* **590**, 411-435(2007).
26. R. Izadi and A. Moosavi, "Electrowetting of power-law fluids in microgrooved channels," *Physics of Fluids* **32**, 073108-1-20(2020).
27. X.-L. Li, G.-W. He and X. Zhang, "Numerical simulation of drop oscillation in AC electrowetting," *Science China Physics, Mechanics and Astronomy*, **56**, 383-394(2013).
28. Y. Guan, B. Y. Li and L. Xing, "Numerical investigation of electrowetting-based droplet splitting in closed digital microfluidic system: Dynamics, mode, and satellite droplet," *Physics of Fluids* **30**, 112001(2018).
29. Z. L. Wang, X. H. Bian and L. G. Chen, "A numerical study of droplet splitting using different spacers in EWOD device," *BioChip Journal*, **14**, 242-250(2020).
30. Y. Yamamoto(山本恭史), T. Ito(伊藤高啓), T. Wakimoto(脇本辰郎) and K. Katoh(加藤健司), "Numerical and theoretical analyses of the dynamics of droplets driven by electrowetting on dielectric in a Hele-Shaw cell," *Journal of Fluid Mechanics* **839**, 468-488(2018).
31. S. F. Kistler, "Hydrodynamics of wetting. In *Wettability* (ed. J.C. Berg)," Marcel Dekker. 311-429 (1993).
32. K. Katoh(加藤健司), T. Wakimoto(脇本辰郎), Y. Ueda(植田芳昭) and M. Iguchi(井口学), "Residual Bubble Volume Formed behind a Sphere Plunging into Liquid Bath (Meniscus Breakdown with Finite Velocity of Sphere Penetration)," *Physics of Fluids* **30**, 082106(2018).